

GT2011-45() \$

A NUMERICAL METHOD FOR TURBULENT FLOWS IN HIGHLY STAGGERED AND LOW SOLIDITY SUPERSONIC TURBINE CASCADES

Shigeki Senoo

Energy and Environmental Systems Laboratory
Power Systems Company
Hitachi, Ltd.
Hitachi, Ibaraki, Japan

Kazuya Sakakibara

Takeshi Kudo
Naoaki Shibashita
Hitachi Works
Power Systems Company
Hitachi, Ltd.
Hitachi, Ibaraki, Japan

ABSTRACT

Two main problems are associated with conventional numerical methods for simulating turbulent flows in high-reaction-type supersonic turbine cascades near the tip of the last stage blade in a steam turbine: the large skewness of computational grids and treatments of boundary conditions when the shock waves hit boundaries. This paper presents a numerical method to deal with these issues.

A grid generation technique which uses five-block structured grids has been developed. The orthogonality of the grid is good even for highly staggered and low solidity cascades. In addition, the grids are completely continuous at the boundary between the blocks and at the periodic boundaries. Both the gradient of the grid lines and the change rate of the grid widths connected smoothly. As a result, shock waves can be captured accurately and stably.

The inflow and outflow boundary conditions based on the two-dimensional characteristic theory have been applied and diminished the spurious reflections and fluctuations of shock waves at both the inlet and outlet boundaries. Therefore the non-physical reflection does not affect the flow in the cascades.

A low Reynolds number $k-\epsilon$ turbulent model has been proposed. Distance from a wall is not used as the characteristic length of turbulent flows so that the turbulent model can be applied to a wake and a separation flow.

The validity of the numerical method was verified by comparisons of the pressure distributions on the blade, the loss coefficients, and flow angles with linear cascade experiments of transonic compressor cascades.

INTRODUCTION

An increase of the annulus area of the last stage in steam turbines has three main benefits: increased power output, improved efficiency, and reduced axial length. When the average axial velocity at the outlet of the larger last stage is almost the same as that of the original last stage, a larger annulus area leads to a larger mass flow rate. The power output can be increased by increasing mass flow rate. When the mass flow rate is almost the same as that of the original turbine, a larger annulus area leads to a smaller average axial velocity at the outlet of the last stage. The efficiency can be improved by reducing the amount of useless kinetic energy. The number of cylinders can be reduced when increment of the annulus area compensates for the annulus area of the original blade. Therefore the length of the blades determines the annulus area and it should be long.

Some technical issues need to be resolved to increase the length of the last blade. One of them is supersonic inflow. Conventionally, outflow Mach numbers are supersonic near the tip of some long blades. Inflow Mach numbers near the tip also become supersonic when the blade is lengthened more. In such cases, it is difficult to avoid emergence of shock waves upstream from the cascade, even if the supersonic turbine aerofoil is applied which has a divergent flow path. The shock waves increase kinetic energy loss by themselves and may cause boundary layer separation which leads to another kinetic energy loss.

Numerical analysis is useful to evaluate such a complex flow, but it has two main issues when applied to the supersonic cascade: large skewness of computational grids and treatments of boundary conditions when the shock waves hit boundaries.

A single H-type structured grid is widely used for flows of a cascade; however, the grid skewness becomes large for highly staggered and low solidity cascades when this type grid is employed. The largely skewed grids destabilize the computation and fail to capture shock waves clearly. The flow comes from almost the peripheral direction near the tip of the lengthened blade in the steam turbine. Therefore stagger angles of the aerofoils are high; some of them are more than 70 degrees. Moreover the solidity is low because the cross-sectional area of the blade is restricted to reduce the centrifugal stresses.

Youngren and Drela [1] improved the single H-type structured grid by using an offset-periodic structure so that the grid skewness was reduced. The implementation of both inlet and outlet boundary conditions, however, became difficult, because the periodicities at the inlet and outlet boundaries vanished.

Shock waves are reflected non-physically at the inlet and outlet boundaries as expansion waves when a normal boundary condition is applied. Chima [2] proposed extrapolation of the one-dimensional Riemann invariant in the main flow direction for supersonic inflow. Giles [3] proposed boundary conditions based on characteristic theory to prevent spurious reflections of waves. However, neither of these authors applied their methods to shock waves.

The purpose of the present paper is to develop a numerical method for turbulent flows in high-reaction-type supersonic cascades, such as the tip section of the long blade in steam turbines. In particular, the paper presents the grid generation technique to reduce the grid skewness and the inflow and outflow boundary conditions to prevent non-physical reflection of shock waves.

GOVERNING EQUATIONS

The governing equations are based on three conservation laws for compressible fluid: mass, momentum and energy.

$$\frac{\partial}{\partial t} \int_V Q dV + \int_{\partial V} (F_j \cdot n_x) dS = \int_{\partial V} (F_{vj} \cdot n_x) dS + P dS_x \quad (1)$$

$$Q = \begin{bmatrix} \rho \\ \rho u \\ \rho v \\ e \end{bmatrix}, \quad F_j = \begin{bmatrix} \rho u_j \\ \rho u u_j + p \delta_{1j} \\ \rho v u_j + p \delta_{2j} \\ (e+p) u_j \end{bmatrix}, \quad F_{vj} = \begin{bmatrix} 0 \\ \tau_{1j} \\ \tau_{2j} \\ q_j \end{bmatrix}, \quad P = \begin{bmatrix} 0 \\ p \\ 0 \\ 0 \end{bmatrix} \quad (2)$$

$$\text{where } e = \rho \left(\hat{\epsilon} + \frac{1}{2} (u^2 + v^2) \right) \quad (3)$$

The stress tensor τ_{ij} consists of the viscous stress μT_{ij} and turbulent stress R_{ij} .

$$\tau_{ij} = \mu T_{ij} - R_{ij} \quad (4)$$

$$T_{ij} = \frac{\partial u_i}{\partial x_j} + \frac{\partial u_j}{\partial x_i} - \frac{2}{3} \frac{\partial u_k}{\partial x_k} \delta_{ij} \quad (5)$$

$$R_{ij} = -\rho \overline{u_i' u_j'} \quad (6)$$

The thermal flux consists of thermal conductivity, work by stress, and turbulent thermal diffusion.

$$q_j = \frac{\lambda}{c_p} \frac{\partial h}{\partial x_j} + \tau_{ij} u_i - \rho \overline{h' u_j'} = \frac{\mu}{Pr} \frac{\partial h}{\partial x_j} + \tau_{ij} u_i - \rho \overline{h' u_j'} \quad (7)$$

The two-dimensional equations are modified regarding the following two points to take into account an axial variation of flow path widths in the blade span direction:

- 1) a pressure term as the fourth term of Eq.(1) and
- 2) hexahedral cells as shown in Fig.1.

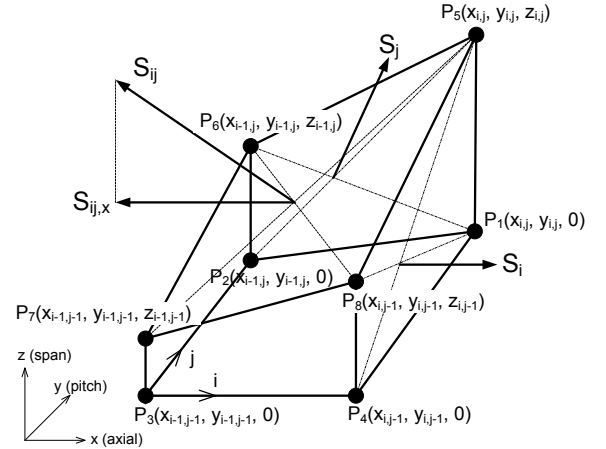


Figure 1. Computational hexahedral cell

The axial and peripheral coordinates of the vertices, x_{ij} and y_{ij} , are two-dimensional functions of a number of grids, i and j . This means all longitudinal sides, such as P_5P_1 in Fig.1, are parallel to the vertical axis, z . The span coordinate, z , is a function of axial coordinate, x , and all z coordinates of lower vertices, such as P_1, P_2, P_3, P_4 , are equal to zero.

The second and third terms in Eq.(1) are integrated over only four side surfaces, S_i, S_j, S_{i-1} , and S_{j-1} in Fig.1.

$S_{ij,x}$ is an axial component of the normal vector of the upper surface, S_{ij} . The dS_x in Eq.(1) for a hexahedral cell equals $-S_{ij,x}$.

TURBULENCE MODEL

A low-Reynolds number type $k-\epsilon$ turbulent model is developed for Reynolds stress and turbulent heat flux based on the work of Shimada and Nagano [4]. Distance from a wall is not used so that the turbulent model can be applied to a wake and a separation flow.

$$R_{ij} \equiv -\rho \overline{u_i' u_j'} = \mu_T T_{ij} - \frac{2}{3} \rho k \delta_{ij} \quad (8)$$

$$-\rho \overline{h' u_j'} = \frac{\lambda_T}{c_p} \frac{\partial h}{\partial x_j} = \frac{\mu_T}{Pr_T} \frac{\partial h}{\partial x_j}, \quad Pr_T = \frac{c_p \mu_T}{\lambda_T} \quad (9)$$

Here μ_T is eddy viscosity and it can be expressed as given below.

$$\mu_T = C_\mu f_\mu \frac{\rho k^2}{\epsilon} \quad (10)$$

$$f_\mu = (1 - f_w) \left\{ 1 + \frac{50}{R_i} \exp \left[- \left(\frac{R_i}{400} \right)^2 \right] \right\} \quad (11)$$

$$f_w = \exp\left(-\frac{R_{tu}^{3/4}}{4500}\right) \quad (12)$$

R_{tu} is a function of time scale ratios of averaged flow R_U and of turbulent flow R_t .

$$R_{tu} = R_U + \left(\frac{f_\gamma \tau_n}{\tau_U}\right) R_t, \quad f_\gamma = \left\{1 - \exp\left[-\left(\frac{R_t}{200}\right)^3\right]\right\} \times 10^3 \quad (13)$$

$$R_U = \frac{u_i u_j \rho k}{\mu \varepsilon} \quad (14)$$

$$R_t = \frac{\rho k^2}{\mu \varepsilon} \quad (15)$$

$$\tau_n = \sqrt{\frac{\mu}{\rho \varepsilon}} \quad (16)$$

$$\tau_U = l/S \quad (17)$$

$$S = \sqrt{S_{ij} S_{ij}}/2 \quad (18)$$

$$S_{ij} = \frac{\partial u_i}{\partial x_j} + \frac{\partial u_j}{\partial x_i} \quad (19)$$

The governing equations for turbulent quantities are written as below.

$$\frac{\partial}{\partial t} \int_V Q^T dV + \int_{\partial V} (F_j^T \cdot n_{x_j}) dS = \int_{\partial V} (F_{vj}^T \cdot n_{x_j}) dS + \int_V I^T dV \quad (20)$$

$$Q^T = \begin{bmatrix} \rho k \\ \rho \varepsilon \end{bmatrix}, \quad F_j^T = \begin{bmatrix} \rho u_j k \\ \rho u_j \varepsilon \end{bmatrix}, \quad F_{vj}^T = \begin{bmatrix} D_{kj} \\ D_{vj} \end{bmatrix}, \quad I^T = \begin{bmatrix} P_k - \rho \varepsilon \\ P_\varepsilon - \varepsilon_\varepsilon \end{bmatrix}$$

$$\hat{F}^T = F_j^T \cdot n_{x_j} = \begin{bmatrix} \rho U k \\ \rho U \varepsilon \end{bmatrix} \quad (21)$$

D_{kj} and D_{vj} are diffusion terms for the turbulent energy and its dissipation rate, respectively, and they are modeled as follows.

$$D_{kj} = \left(\mu + \frac{\mu_T}{\sigma_k^*}\right) \frac{\partial k}{\partial x_j}, \quad \sigma_k^* = \frac{1.2}{f_t} \quad (22)$$

$$D_{vj} = \left(\mu + \frac{\mu_T}{\sigma_\varepsilon^*}\right) \frac{\partial \varepsilon}{\partial x_j}, \quad \sigma_\varepsilon^* = \frac{1.3}{f_t} \quad (23)$$

$$f_t = 1 + 20 \exp\left(-\frac{R_t}{30}\right) \quad (24)$$

P_k is production of turbulent energy and it is modeled using the velocity gradient tensor and vorticity tensor.

$$P_k = \mu_T S \Omega, \quad S = \sqrt{S_{ij} S_{ij}}/2, \quad \Omega = \sqrt{\Omega_{ij} \Omega_{ij}}/2, \quad (25)$$

$$\Omega_{ij} = \frac{\partial u_i}{\partial x_j} - \frac{\partial u_j}{\partial x_i} \quad (26)$$

P_ε , ε_ε and E are production, dissipation and correction terms of ε , respectively, and they are modeled as follows.

$$P_\varepsilon = C_{\varepsilon 1} f_{\varepsilon 1} \frac{\varepsilon}{k} P_k \quad (27)$$

$$\varepsilon_\varepsilon = C_{\varepsilon 2} f_{\varepsilon 2} \frac{\rho \varepsilon^2}{k} \quad (28)$$

$$f_{\varepsilon 1} = 1 + 0.4 \exp\left[-2 \times 10^{-6} \left(\frac{u_i u_i}{k}\right)^4\right] \quad (29)$$

$$f_{\varepsilon 2} = \left\{1 - 0.3 \exp\left[-\left(\frac{R_t}{6.5}\right)^2\right]\right\} \left[1 - \exp\left(-\frac{R_{tu}^{1/4}}{1.5}\right)\right]^2 \quad (30)$$

The four constants of the turbulence model are tuned as shown in Table 1 to match the experimental results of a turbulent boundary layer on a flat plate and flows in linear cascades [5].

Table 1. Constants of the turbulence model

C_μ	$C_{\varepsilon 1}$	$C_{\varepsilon 2}$	Pr_T
0.09	1.45	1.9	0.9

NUMERICAL METHOD

Equation (1) is solved using a finite volume method based on the third-order upwind TVD scheme [5, 6]. A diagonal form of the implicit approximate factorization algorithm [7] is applied for time integration.

GRID GENERATION

A grid generation technique using the five-block structured grids is developed. A grid configuration is shown in Fig.2. A block ① with an offset-periodic structured grid is applied around the blades to improve the orthogonality of the generated grids. Two blocks, ② and ③, with a structured grid, are inserted into the inlet triangular region to make the inlet line of computational region parallel to the peripheral direction. The last two blocks, ④ and ⑤, are inserted into an outlet triangular region.

First, block boundaries and periodic boundaries are generated and divided into grids. The number of the offset value of the grid between suction and pressure surfaces is determined as follows. The grid number of the pressure surface, ix_throat_ps in Fig.2, is calculated so that the distance from the leading edge of the suction surface is minimized. The *offset* is the difference between ix_throat_ps and the grid number at the inlet region of the suction surface, ixi ,

$$offset = ix_throat_ps - ixi. \quad (31)$$

Second, the numbers of grids of the inlet blocks ② and ③ as shown in Fig.3, are determined so that the grids are completely continuous at the boundary between the blocks. Three conditions, given as Eqs. (32) to (34), should be preserved.

$$NY1 = NX2 + NY3 \quad (32)$$

$$offset = NX2 + NX3 \quad (33)$$

$$NY2 = NX3 + NY3 \quad (34)$$

Only one parameter is free when *offset* and *NY1* are specified because there are four unknowns and three constraints. These conditions (32) to (34) lead to the following relation.

$$NX2 = \frac{NY1}{2} + \frac{offset}{2} (1 - r_{gin}), \quad r_{gin} \equiv \frac{NY2}{offset} \quad (35)$$

The controllable parameter is the ratio r_{gin} between the number of inlet grids *NY2* and the *offset* in this study.

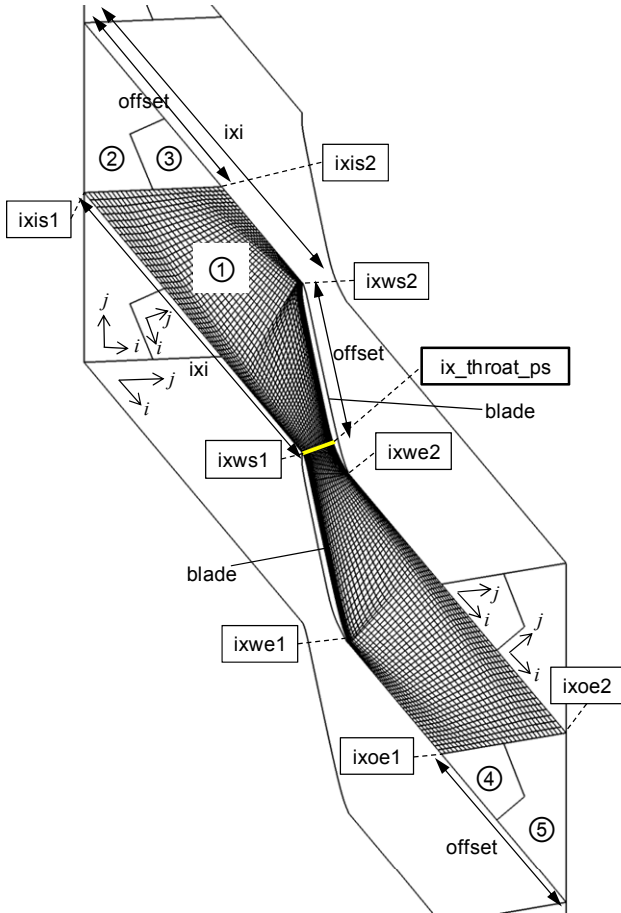


Figure 2. Five-block structured grids

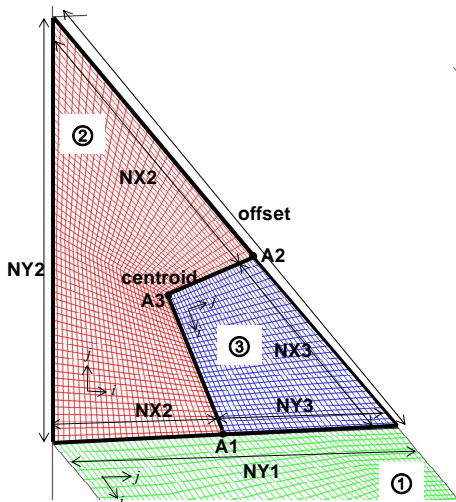


Figure 3. Inlet region grids

Third, the inlet triangle region is divided into ② and ③. The grids are equally divided at the boundary with block ①; therefore $A1$ is determined using the ratio $NX2:NY3$. The grids of the periodic boundaries have already been divided to match

the corresponding grids of block ①; therefore $A2$ is determined using the ratio $NX2:NX3$. $A3$ is determined as the centroid of the inlet triangle. The inlet boundary is equally divided by $NY2$.

Fourth, the outlet blocks ④ and ⑤ are determined in the same way as the inlet blocks ② and ③.

Finally the smooth inner grids are generated using Poisson equations [8]. Both the gradient of grid lines and the change rate of grid width connect smoothly at the block boundaries and periodic boundaries by formulating the source term of the Poisson equations.

The other advantage of the grid generation method is its small number of input parameters. By adding only two parameters, r_{gin} and r_{gout} , to the input parameters of single H-type grids, the five-block structured grids can be generated. The developed grid generation method easily replaces a single H-type grid generation method, because the same values are applied for most of the common input parameters.

The method is applied to generate grids of cascades with stagger angle 76.5 degree. The results are shown in Fig. 4. The orthogonality of the grid is good even for highly staggered and low solidity cascades. In addition, the grids are completely continuous at the boundaries between the blocks and at the periodic boundaries. The gradient of grid lines and the change rate of grid width connect smoothly.

Figure 5 compares computational grids between the developed five-block structured grids and the widely-used single H-type grids. The orthogonality of the grids is improved. Figure 6 compares iso-pressure contours of inviscid flow calculations. Both results can simulate the same shock wave pattern. In the five-block grids, however, shock waves can be captured more accurately and they propagate through the block and periodic boundaries without the attenuation which may occur if there are grid discontinuities.

INFLOW AND OUTFLOW BOUNDARY CONDITIONS

Inflow and outflow boundary conditions are based on the two-dimensional characteristic theory proposed by Giles [3]. There are two features to suppress spurious reflections. One is that peripheral variations of physical quantities are allowed at boundaries. The other is that incoming two-dimensional waves of perturbations are set as zero. The ideal gas is assumed for the working fluid in this paper to formulate the boundary conditions.

First of all, independent variables of governing equations are transformed from conservative variables to one-dimensional characteristic variables. Two-dimensional Euler equations in the Cartesian coordinate system are used in this capture, because the grids are orthogonal and both viscosity and turbulence are not so important at the inlet and outlet boundaries. Two-dimensional Euler equations can be expressed in the differential form given below.

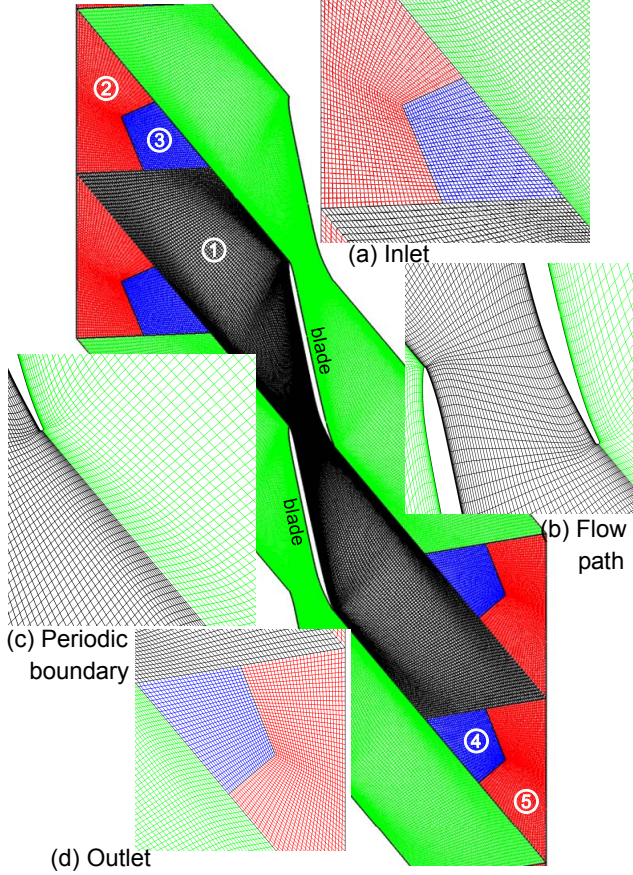


Figure 4. Computational grids

$$\frac{\partial}{\partial t} \begin{bmatrix} \rho \\ \rho u \\ \rho v \\ e \end{bmatrix} + \frac{\partial}{\partial x} \begin{bmatrix} \rho u \\ \rho u^2 + p \\ \rho uv \\ eu + pu \end{bmatrix} + \frac{\partial}{\partial y} \begin{bmatrix} \rho v \\ \rho v^2 + p \\ \rho uv \\ ev + pv \end{bmatrix} = 0 \quad (36)$$

The conservative variables are transformed to primitive variables to simplify the eigenvalue calculation.

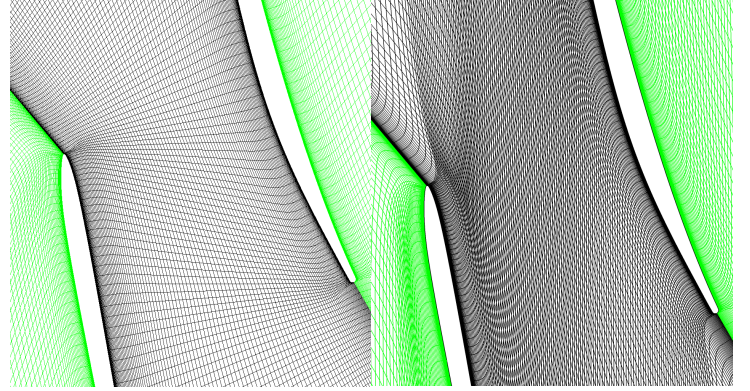
$$\begin{bmatrix} d\rho \\ du \\ dv \\ dp \end{bmatrix} = \begin{bmatrix} 1 & 0 & 0 & 0 \\ -u/\rho & -1/\rho & 0 & 0 \\ -v/\rho & 0 & -1/\rho & 0 \\ (\gamma-1)(u^2+v^2)/2 & -(\gamma-1)u & -(\gamma-1)v & \gamma-1 \end{bmatrix} \begin{bmatrix} d\rho \\ d(\rho u) \\ d(\rho v) \\ de \end{bmatrix} \quad (37)$$

By using this, Eq. (36) can be written in the non-conservative form given below

$$\frac{\partial}{\partial t} \begin{bmatrix} \rho \\ u \\ v \\ p \end{bmatrix} + \begin{bmatrix} u & \rho & 0 & 0 \\ 0 & u & 0 & 1/\rho \\ 0 & 0 & u & 0 \\ 0 & \gamma p & 0 & u \end{bmatrix} \frac{\partial}{\partial x} \begin{bmatrix} \rho \\ u \\ v \\ p \end{bmatrix} + \begin{bmatrix} v & 0 & \rho & 0 \\ 0 & v & 0 & 0 \\ 0 & 0 & v & 1/\rho \\ 0 & 0 & \gamma p & v \end{bmatrix} \frac{\partial}{\partial y} \begin{bmatrix} \rho \\ u \\ v \\ p \end{bmatrix} = 0 \quad (38)$$

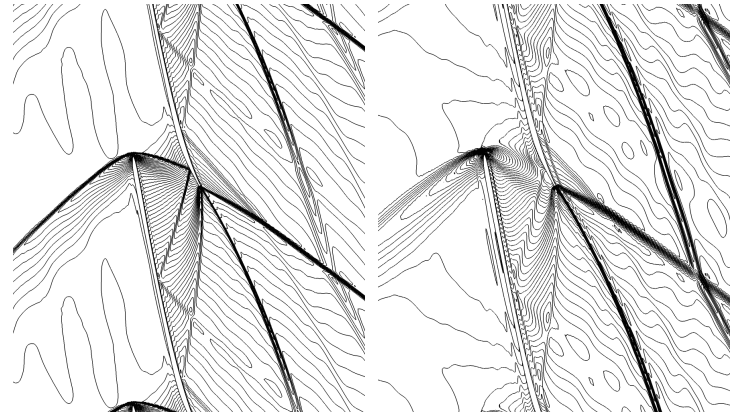
The vector of peripheral perturbation is used to define U .

$$U = \begin{bmatrix} \tilde{\rho} \\ \tilde{u} \\ \tilde{v} \\ \tilde{p} \end{bmatrix} \equiv \begin{bmatrix} \rho - \bar{\rho} \\ u - \bar{u} \\ v - \bar{v} \\ p - \bar{p} \end{bmatrix} \quad (39)$$



(a) Five-block structured grid (b) Single H-type grid

Figure 5. Comparison of computational grids



(a) Five-block structured grid (b) Single H-type grid

Figure 6. Comparison of iso-pressure contours of two different types of grids

Here the tilde denotes the peripheral perturbation and the overline denotes the peripheral average. Then, Eq. (38) can be linearized by neglecting all but the first order linear terms.

$$\frac{\partial U}{\partial t} + A \frac{\partial U}{\partial x} + B \frac{\partial U}{\partial y} = 0 \quad (40)$$

$$A = \begin{bmatrix} u & \rho & 0 & 0 \\ 0 & u & 0 & 1/\rho \\ 0 & 0 & u & 0 \\ 0 & \gamma p & 0 & u \end{bmatrix}, \quad B = \begin{bmatrix} v & 0 & \rho & 0 \\ 0 & v & 0 & 0 \\ 0 & 0 & v & 1/\rho \\ 0 & 0 & \gamma p & v \end{bmatrix} \quad (41)$$

A vector of the one-dimensional characteristic variables C can be calculated from primitive variables using the eigenvalue decomposition of Jacobian matrix A .

$$A = R\Lambda L \quad (42)$$

$$C = \begin{bmatrix} c_1 \\ c_2 \\ c_3 \\ c_4 \end{bmatrix} = LU = \begin{bmatrix} w_1^L \\ w_2^L \\ w_3^L \\ w_4^L \end{bmatrix} U = \begin{bmatrix} -a^2 & 0 & 0 & 1 \\ 0 & 0 & \rho a & 0 \\ 0 & \rho a & 0 & 1 \\ 0 & -\rho a & 0 & 1 \end{bmatrix} \begin{bmatrix} \rho \\ u \\ v \\ p \end{bmatrix} \quad (43)$$

$$U = RC = \begin{bmatrix} w_1^R & w_2^R & w_3^R & w_4^R \end{bmatrix} C = \begin{bmatrix} -1/a^2 & 0 & 1/2a^2 & 1/2a^2 \\ 0 & 0 & 1/2\rho a & -1/2\rho a \\ 0 & 1/\rho a & 0 & 0 \\ 0 & 0 & 1/2 & 1/2 \end{bmatrix} \begin{bmatrix} c_1 \\ c_2 \\ c_3 \\ c_4 \end{bmatrix} \quad (44)$$

Here L and R are the matrices consisting of left and right eigenvectors w_n^L and w_n^R of the Jacobian matrix A , respectively.

Inflow Conditions

One-dimensional characteristic variables are corrected step-by-step until they satisfy the given conditions. A conceptual diagram of inflow boundary conditions is shown in Fig. 7. Three one-dimensional characteristic variables are divided into the peripheral average (overline) and the perturbation (tilde) at the boundary to take into account the peripheral variations.

First, the average value should be satisfied with given boundary conditions at far-field. Stagnation pressure P_0 , stagnation temperature T_0 , and inlet flow angle α_{in} are specified at far-field. Stagnation entropy and stagnation enthalpy calculated by P_0 and T_0 do not change from far-field to the inlet boundary. Therefore corrections of average values can be expressed as the following.

$$\left. \begin{aligned} R_1 &= \bar{\rho} (\bar{s} - s_0) \\ R_2 &= \bar{\rho} \bar{a} [v_F - \tan(\alpha_{in}) u_F] \\ R_3 &= \bar{\rho} [\bar{H} - H_0] \end{aligned} \right\} \quad (45)$$

Here the subscript F means a value at far-field. The corrections in Eq. (45) are transformed to one-dimensional characteristic variables [9].

$$\begin{bmatrix} \delta \bar{c}_1 \\ \delta \bar{c}_2 \\ \delta \bar{c}_3 \end{bmatrix} = \frac{-1}{1 + M_x + M_y \tan(\alpha_{in})} \times \begin{bmatrix} 1 + M_x + M_y \tan(\alpha_{in}) & 0 & 0 \\ \frac{-1}{\gamma - 1} \tan(\alpha_{in}) & 1 + M_x & \tan(\alpha_{in}) \\ \frac{-2}{\gamma - 1} & -2M_y & 2 \end{bmatrix} \begin{bmatrix} R_1 \\ R_2 \\ R_3 \end{bmatrix} \quad (46)$$

Here M_x and M_y are Mach numbers in axial and peripheral directions, respectively.

Second, the incoming two-dimensional characteristic waves of perturbation variables should be zero to suppress non-physical reflection. To clarify the propagating direction, the solutions of Eq. (40) are decomposed into two-dimensional characteristic waves. Steady two-dimensional spatial-wave-like solutions can be written using wave numbers k and l .

$$U(x, y) = u e^{i(kx + ly)} \quad (47)$$

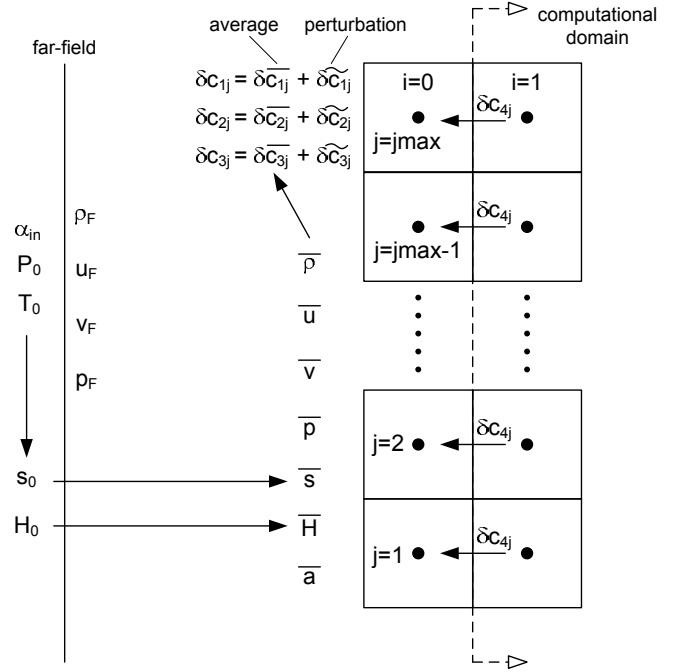


Figure 7. Conceptual diagram of inlet boundary conditions

Substituting this into the linearized steady perturbation equations of (40) gives the dispersion relationship.

$$(kA + lB)u = 0 \rightarrow \det(kA + lB) = 0 \quad (48)$$

Therefore the wave numbers k and l are not independent of each other.

Waves propagate in the axial direction at the inlet and outlet boundaries, because the boundaries are perpendicular to the axial direction. Therefore solutions to Eq. (47) are decomposed into a sum of two-dimensional waves with the axial wave number k_n with different peripheral wave number l .

$$U(x, y) = \left[\sum_{n=1}^4 a_n v_n^R e^{i k_n x} \right] e^{i l y} \quad (49)$$

Here v_n^R is the right eigenvector of the matrix $(k_n I + l A^{-1} B)$ and a_n is the amplitude. The axial wave number k_n ($n=1, 2, 3, 4$) is determined as the n th root of the dispersion relation Eq. (48) for the given peripheral wave number l . Therefore, each one of four two-dimensional characteristic waves propagating in the axial direction can be extracted by multiplying the left eigenvectors v_n^L of the matrix $(k_n I + l A^{-1} B)$ as $v_n^L U(x, y) = a_n e^{i(k_n x + l y)}$ due to the orthogonality relation of the eigenvectors between v_n^R and v_n^L . Three of four waves are incoming, because their eigenvalues are positive, when the axial velocity is subsonic. Therefore nonreflecting boundary conditions that the incoming two-dimensional characteristic waves of perturbation variables should be zero can be written as given below.

$$\begin{bmatrix} v_1^L \\ v_2^L \\ v_3^L \end{bmatrix} U = \begin{bmatrix} -a^2 & 0 & 0 & 1 \\ 0 & -u & -v & -\frac{1}{\rho} \\ 0 & -v & u & \frac{\beta}{\rho a} \end{bmatrix} \begin{bmatrix} \tilde{p} \\ \tilde{u} \\ \tilde{v} \\ \tilde{p} \end{bmatrix} = 0 \quad (50)$$

β is the parameter depending on the velocity.

$$\beta = \begin{cases} i \operatorname{sign}(l) \sqrt{a^2 - (u^2 + v^2)}, & u^2 + v^2 < a^2 & \text{subsonic} \\ -\operatorname{sign}(v) \sqrt{(u^2 + v^2) - a^2}, & u^2 + v^2 > a^2 & \text{supersonic} \end{cases} \quad (51)$$

The β is independent of the peripheral wave number l when the velocity is supersonic. Therefore the condition (50) is also independent of the peripheral wave number for supersonic flows.

The condition (50) is transformed to the function of the one-dimensional characteristics using Eq. (44).

$$\begin{bmatrix} v_1^L \\ v_2^L \\ v_3^L \end{bmatrix} U = \begin{bmatrix} v_1^L \\ v_2^L \\ v_3^L \end{bmatrix} RC = \begin{bmatrix} 1 & 0 & 0 & 0 \\ 0 & -v & -\frac{1}{2}(a+u) & -\frac{1}{2}(a-u) \\ 0 & u & \frac{1}{2}(\beta-v) & \frac{1}{2}(\beta+v) \end{bmatrix} \begin{bmatrix} \tilde{c}_1 \\ \tilde{c}_2 \\ \tilde{c}_3 \\ \tilde{c}_4 \end{bmatrix} = 0 \quad (52)$$

Therefore three incoming two-dimensional characteristic waves of perturbation variables should be satisfied with the following equation which can be obtained by solving Eq. (52) to obtain three incoming characteristics as a function of the outgoing ones.

$$\begin{bmatrix} \tilde{c}_1 \\ \tilde{c}_2 \\ \tilde{c}_3 \end{bmatrix} = \begin{bmatrix} 0 \\ -\left(\frac{\beta+v}{a+u}\right) \tilde{c}_4 \\ \left(\frac{\beta+v}{a+u}\right)^2 \tilde{c}_4 \end{bmatrix} \quad (53)$$

The outgoing characteristic is given as Eq. (54) from Eq.(43).

$$\tilde{c}_4 = -\rho a \tilde{u} + \tilde{p} \quad (54)$$

Therefore the steady-state correction to the local incoming characteristic of perturbation variables can be calculated as the difference between the correct steady-state value of Eq. (53) and the current value of Eq. (43).

$$\begin{cases} \delta \tilde{c}_1|_{i=0,j} = \tilde{c}_1|_{i=0,j} - \tilde{c}_1|_{i=0,j} \\ \delta \tilde{c}_2|_{i=0,j} = \tilde{c}_2|_{i=0,j} - \tilde{c}_2|_{i=0,j} \\ \delta \tilde{c}_3|_{i=0,j} = \tilde{c}_3|_{i=0,j} - \tilde{c}_3|_{i=0,j} \end{cases} \quad (55)$$

Then, by using Eq. (53), Eq. (56) is obtained.

$$\begin{cases} \tilde{c}_{1s}|_{i=0,j} = 0 \\ \tilde{c}_{2s}|_{i=0,j} = \left[-\frac{\beta + M_y}{I + M_x} \tilde{c}_4 \right]_{i=0,j}, \quad \beta = -\operatorname{sign}(v) \sqrt{M^2 - 1} \\ \tilde{c}_{3s}|_{i=0,j} = \left[\left(\frac{\beta + M_y}{I + M_x} \right)^2 \tilde{c}_4 \right]_{i=0,j} \end{cases} \quad (56)$$

Further, by using Eq. (43), Eq. (57) is obtained.

$$\begin{cases} \tilde{c}_1|_{i=0,j} = [-a^2 \tilde{p} + \tilde{p}]_{i=0,j} \\ \tilde{c}_2|_{i=0,j} = [\rho a \tilde{v}]_{i=0,j} \\ \tilde{c}_3|_{i=0,j} = [\rho a \tilde{u} + \tilde{p}]_{i=0,j} \end{cases} \quad (57)$$

Third, the total local correction which is the sum of the peripherally averaged and perturbative characteristic variable is calculated using Eqs. (46) and (55).

$$\begin{cases} \delta c_1|_{i=0,j} = \sigma_0 \left(\delta \tilde{c}_1|_{i=0,j} + \delta \tilde{c}_1|_{i=0,j} \right) \\ \delta c_2|_{i=0,j} = \sigma_0 \left(\delta \tilde{c}_2|_{i=0,j} + \delta \tilde{c}_2|_{i=0,j} \right) \\ \delta c_3|_{i=0,j} = \sigma_0 \left(\delta \tilde{c}_3|_{i=0,j} + \delta \tilde{c}_3|_{i=0,j} \right) \end{cases} \quad (58)$$

σ_0 is the under-relaxation factor to guarantee the well-posedness of the mathematical formulation [9]. In this paper, the following formula is applied for σ_0 .

$$\sigma_0 = \min \left[0.5, \frac{10}{j \max} \right] \quad (59)$$

Finally, the correction of the fourth characteristic variable δc_4 is extrapolated from the calculated region.

Outflow Conditions

The fourth characteristic variable is only the incoming wave at the outlet boundary because its eigenvalue is negative. It is divided into the peripheral average and the perturbation.

First, the average should satisfy the given static pressure at far-field.

Second, the perturbation should satisfy the condition where the incoming two-dimensional characteristic wave vanishes. The condition can be expressed similarly to Eq. (50) as the condition (60)

$$v_4^L U = \begin{bmatrix} 0 & v & -u & \frac{\beta}{\rho a} \end{bmatrix} \begin{bmatrix} \tilde{p} \\ \tilde{u} \\ \tilde{v} \\ \tilde{p} \end{bmatrix} = 0 \quad (60)$$

It is transformed to the function of the one-dimensional characteristics using Eq. (44).

$$v_4^L U = v_4^L RC = \begin{bmatrix} 0 & -u & \frac{1}{2}(\beta+v) & \frac{1}{2}(\beta-v) \end{bmatrix} \begin{bmatrix} \tilde{c}_1 \\ \tilde{c}_2 \\ \tilde{c}_3 \\ \tilde{c}_4 \end{bmatrix} = 0 \quad (61)$$

Therefore the fourth incoming two-dimensional characteristic waves of perturbation variables should be satisfied with the following expression.

$$\tilde{c}_4 = \left(\frac{2u}{\beta - v} \right) \tilde{c}_2 - \left(\frac{\beta + v}{\beta - v} \right) \tilde{c}_3 \quad (62)$$

$$\begin{cases} \tilde{c}_2 = -\rho a \tilde{v} \\ \tilde{c}_3 = \rho a \tilde{u} + \tilde{p} \end{cases} \quad (63)$$

The definitions of Eq. (63) are gotten from Eq.(43).

The other three characteristic variables are extrapolated from the calculated region.

Computational Results

Three types of boundary conditions are compared. 1) Normal: extrapolate the axial velocity at the inlet and the density, axial and peripheral momentums at the outlet; 2) 1D Riemann: extrapolate the one-dimensional Riemann invariant at the inlet as proposed by Chima [2]; and 3) 2D characteristic: use the aforementioned method. The combinations of boundary conditions are shown in Table 2.

Table 2. Inflow and outflow boundary conditions

Case	Boundary conditions		Axial positions	
	inflow	outflow	inlet	outlet
1	normal	normal	9.6	9.6
2	1D Riemann	normal	9.6	9.6
3	2D characteristic	2D characteristic	9.6	9.6
4	normal	normal	4.8	4.8
5	2D characteristic	2D characteristic	4.8	4.8

Axial positions in Table 2 are distances normalized by the axial chord length from the inlet boundary to the leading edge of the blade for the inlet and from the outlet boundary to the trailing edge for the outlet.

The inflow Mach number is 1.3 and the outflow isentropic Mach number is 2.1. The iso-pressure contours are compared in Fig.8. The oblique shocks non-physically reflect as expansion waves which affect the flow in the cascade in cases 1 and 2. The spurious reflections are slight and do not affect the flow in the cascade in case 3. The non-physical fluctuation occurs at the outlet boundary due to the interactions with oblique shocks in cases 1 and 2. However it does not occur in case 3. As a result, the developed boundary conditions are validated.

The effect of the computational region is also studied. The inlet and outlet region are reduced by half for cases 4 and 5 as shown in Table 2. The iso-pressure contours are shown in Fig. 9 where the shortened cases are at the mid flow paths. The spurious reflections at the inlet boundary become stronger but they still do not affect the flow in the cascade in case 5. However the non-physical fluctuation occurs at the outlet boundary even in case 5. This means that the outlet boundary cannot be reduced from that of case 3.

VALIDATIONS

The developed numerical technique is validated by comparisons with linear cascade experiments. Experimental data obtained by DFVRL are used including two types of transonic compressor cascades, DFVRL [10] and ARL-SL19 [11], because there are no experimental data for supersonic turbine cascades. Working fluid is air. Thermal boundary conditions are shown in Table 3. AVDR is an acronym standing for Axial Velocity Density Ratio, which is defined as (64).

$$AVDR = \frac{\rho_{out} u_{out}}{\rho_{in} u_{in}} \quad (64)$$

The calculated contours of Mach number are shown in Fig. 10. Shock waves are captured accurately and do not reflect non-physically at the inlet boundary. The supersonic flows come into the DFVLR compressor cascades and detached shock waves emerge in front of the leading edge. After the shock waves the velocity becomes subsonic.

Table 3. Thermal boundary conditions

Parameters	Unit	Case 6	Case 7	Case 8
Blade type	-	DFVLR	DFVLR	ARL-SL19
Inlet Mach number	-	1.03	1.10	1.58
Inlet flow angle	deg	148.5	148.5	147.5
Static pressure ratio	-	1.47	1.57	2.12
AVDR	-	1.14	1.15	0.99

The higher supersonic flows come into the ARL-SL19 compressor cascades and generate oblique shock waves in the flow path of cascades. The flow does not decelerate to subsonic after the shock waves; therefore rather it accelerates again in the divergent flow path. The normal shock waves emerge at the trailing edges and interact with the boundary layer on the pressure surface. The interaction causes local separation of the boundary layer which leads to the oscillation of the shock waves. As a result, the flow becomes unsteady especially in the subsonic region after the normal shock waves.

Comparisons of pressure coefficient distributions on the blade surface, which are defined as (65), are shown in Fig. 11 for the DFVLR cascades. The agreements are good including the impingement positions of shock waves on the suction surfaces.

$$C_p = \frac{P_{0in} - p}{P_{0in} - p_{in}} \quad (65)$$

The comparison of isentropic Mach number distributions on the blade surface is shown in Fig.12. The averaged result is used for the computational result and again, it agrees well with the experimental. However there are two differences between the computation and the experiment. One is that the experimental flow accelerates again after the impingement of the oblique shock waves on the suction surface; while on the other hand, the isentropic Mach number of the computation is almost constant from the shock wave impingement to the trailing edge due to the separation of the boundary layer.

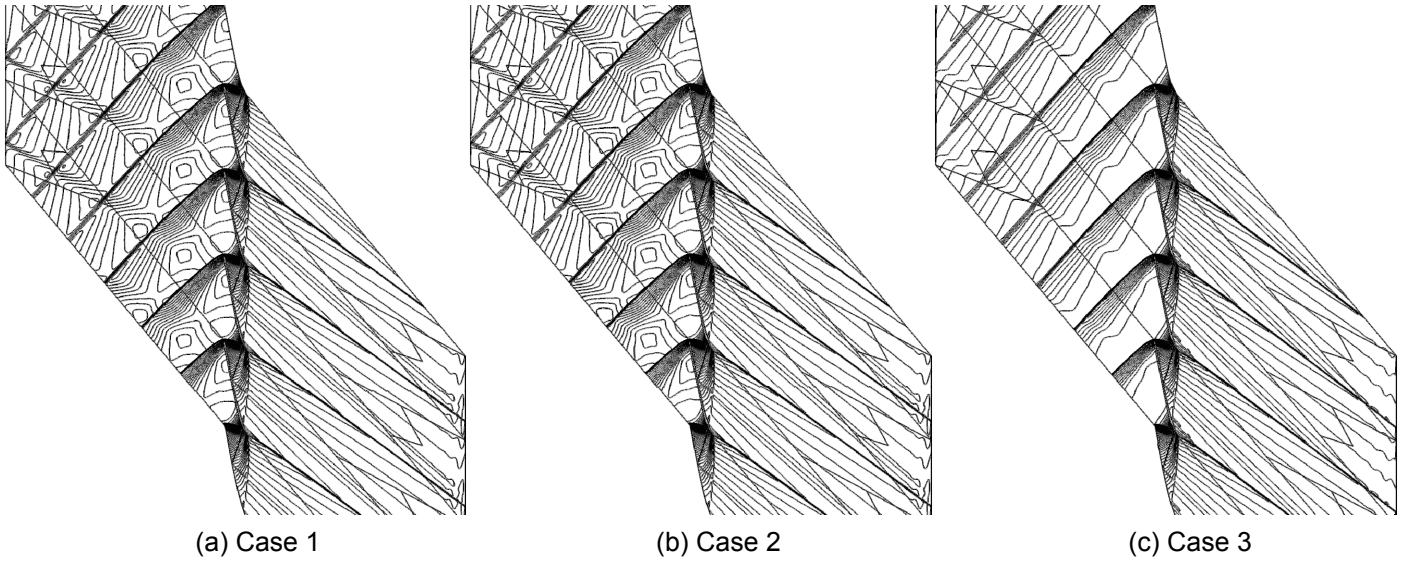


Figure 8. Comparison of iso-pressure contours of different boundary conditions

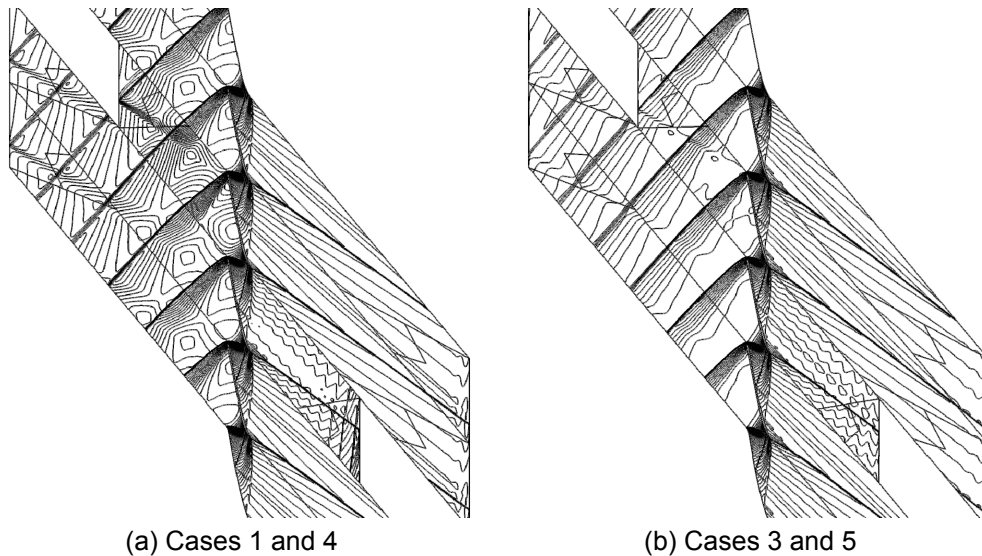


Figure 9. Comparison of iso-pressure contours of different computational regions

The other is that the deceleration of the computation on the pressure surface caused by the impingement of the normal shock waves is steeper than that of the experiment. These differences may be caused by the inadequacy of the turbulence model in dealing with the strong interaction between a shock wave and a boundary layer.

Comparison of total pressure loss coefficient, which is defined by (66) and outlet flow angle is shown in Table 4 for three calculation cases.

$$\omega = \frac{P_{0in} - P_{0out}}{P_{0in} - p_{in}} \quad (66)$$

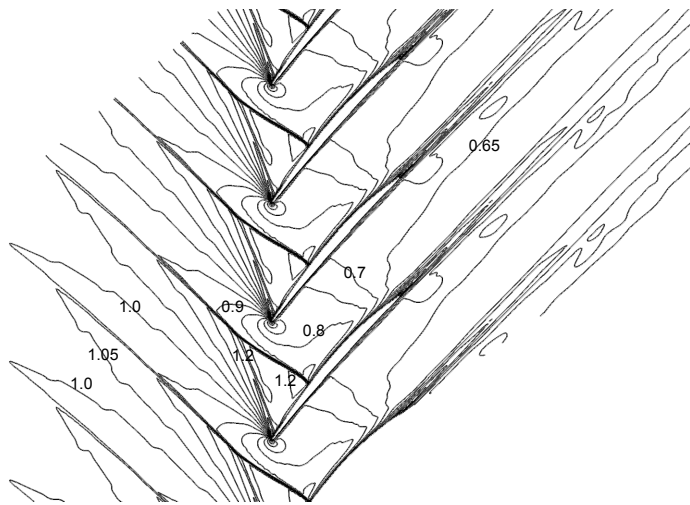
The computational total loss coefficients are less than the computational ones by about 2% in cases 6 and 7. The average total loss coefficient agrees with the experimental one in case 8.

The agreement of the outlet flow angles of the computation with those of the experiment can be confirmed.

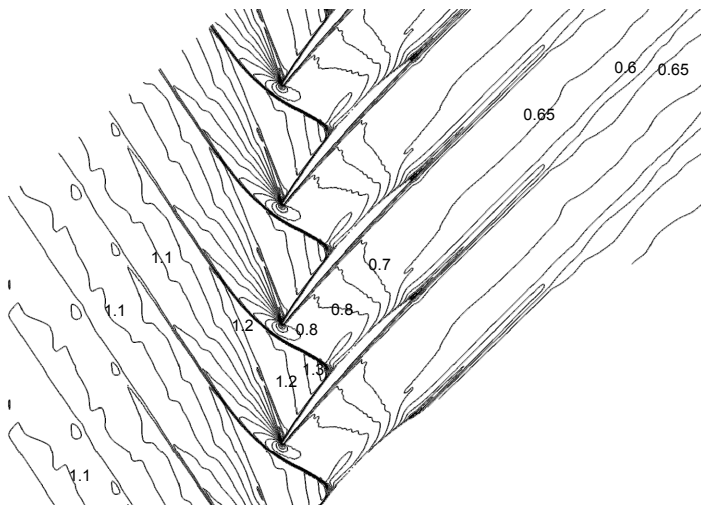
Table 4. Comparison of loss coefficient and outlet flow angle

Parameters	Unit		Case 6	Case 7	Case 8
Loss coefficient	%	CFD	4.3	6.5	14.6
		Exp	6.1	8.4	14.4
Outlet flow angle	deg	CFD	135.7	135.2	153.0
		Exp	136	136	151.2

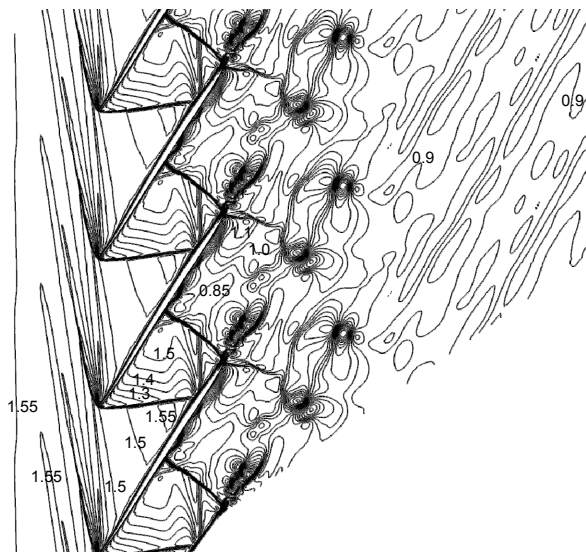
In conclusion, the validity of the developed numerical method is verified.



(a) Case 6 (DFVLR $M_{in}=1.03$)

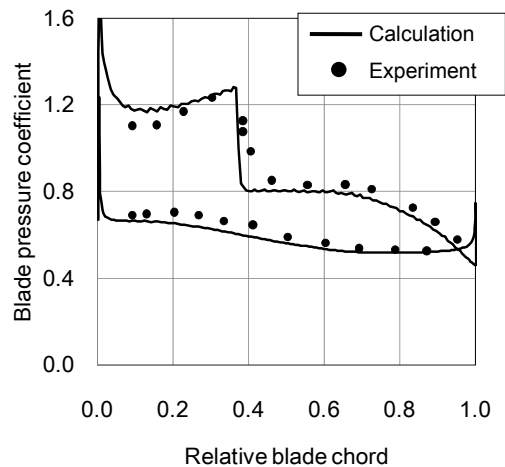


(b) Case 7 (DFVLR $M_{in}=1.10$)

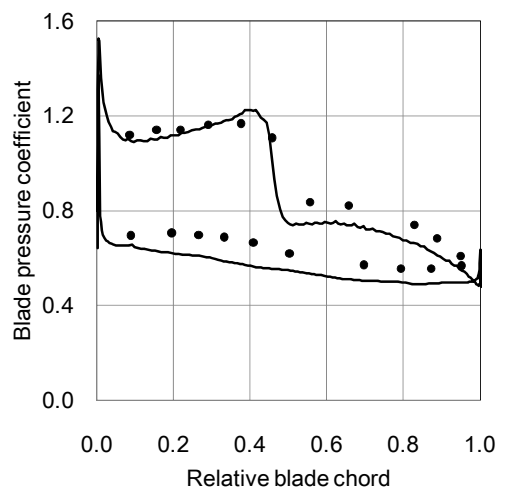


(c) Case 8 (ARL-SL19 $M_{in}=1.58$)

Figure 10. Iso Mach number contours (increments 0.05)



(a) Case 6 (DFVLR $M_{in}=1.03$)



(b) Case 7 (DFVLR $M_{in}=1.1$)

Figure 11. Pressure coefficient distributions on the blade surface

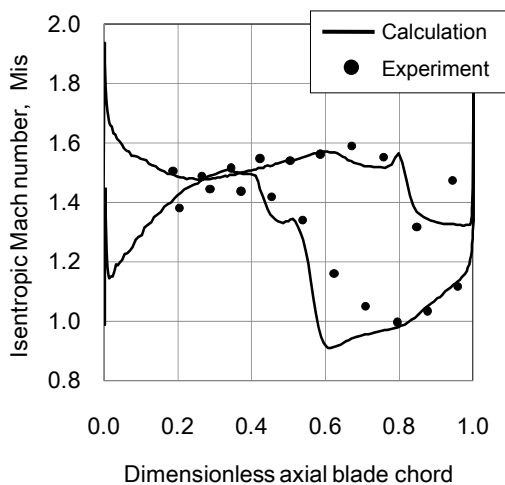


Figure 12. Isentropic Mach number distributions on the blade surface Case 8 (ARL-SL19 $M_{in}=1.58$)

CONCLUSIONS

The numerical methods for treating turbulent flows in high-reaction-type supersonic cascades were developed.

The five-block structured grid generation technique could generate grids with better orthogonality even for highly staggered and low solidity cascades. It was able to capture the shock waves accurately and stably. The grids were completely continuous at the boundaries between blocks and the periodic boundaries by using the offset-periodic technique. In addition, the Poisson equations were used to generate smooth grids in the blocks and their source terms are formulated so that the gradient of the grid lines and the change rate of the grid widths connect smoothly. Therefore shock waves did not attenuate at the boundaries.

Nonreflecting boundary conditions based on two-dimensional characteristic theory were applied for supersonic inflow and outflow. The physical quantities were separated into the circumferential average and the perturbation at the boundaries. The average quantities were decided by given values at a hypothetical far-field. The amplitude of incoming two-dimensional characteristic waves of the perturbations is set to zero to suppress nonphysical reflections of waves. In this way the computations avoid spurious reflections of shock waves at the inlet and outlet boundaries.

The equations of conservation laws for compressible fluid were used in consideration of an axial variation of span width of the flow path to take into account quasi-three-dimensional effects. The equations are solved by using a finite volume method based on an approximate Riemann solver. A low Reynolds number k - ϵ turbulent model was proposed for flows of 10^5 - 10^6 order Reynolds number.

The flows of two types of transonic compressor cascades were calculated and the results were compared with those of linear cascade experiments. The computational pressure distributions and positions of shock waves on the blade agreed well with the experiments. The prediction accuracy of outlet flow angles was good. The estimated total pressure losses in the transonic cascade with a convex suction surface were about 2% smaller compared with the experimental results. However the computation accurately predicted the total pressure loss in the transonic cascade with a concave suction surface. The validity of the numerical method was verified from the above findings.

It was confirmed that the developed numerical method was sufficiently accurate for applications to design of supersonic turbine cascades, such as the tip section of the long blade in steam turbines.

NOMENCLATURE

- A Jacobian matrix with respect to x , Eq. (41)
 a sound velocity
 B Jacobian matrix with respect to y , Eq. (41)
 C one-dimensional characteristic variables vector

- C_p pressure coefficient on the blade surface
 c_p specific heat capacity at constant pressure
 e total energy per unit volume
 h specific enthalpy
 k turbulent energy per unit volume
 k wave number of x direction
 L matrix consisting of left eigenvector of matrix A
 l wave number of y direction
 M Mach number
 n_{xj} normal vector relative to the grid surface
 P_0 stagnation pressure
 p static pressure
 Pr Prandtl number
 Pr_T turbulent Prandtl number
 Q conservative variables
 R matrix consisting of right eigenvector of matrix A
 R_{ij} Reynolds stress tensor
 S surface area of computational cells
 S magnitude of velocity gradient tensor, Eq. (18)
 S_{ij} velocity gradient tensor, Eq. (19)
 T_0 stagnation temperature
 U peripheral perturbation vector of primitive variables
 u, v axial and peripheral velocities
 V volume of computational cells
 v_n^L left eigenvector of matrix $(k_n I + l A^{-1} B)$
 v_n^R right eigenvector of matrix $(k_n I + l A^{-1} B)$
 w_n^L left eigenvector of matrix A
 w_n^R right eigenvector of matrix A
 x axial direction
 y peripheral direction

Greek symbols

- ϵ dissipation rate of turbulent energy per unit volume
 $\hat{\epsilon}$ specific internal heat
 γ specific heat rate
 λ thermal conductivity
 λ_T turbulent thermal conductivity
 μ dynamic viscosity
 μ_T eddy viscosity
 ρ density
 τ_{ij} stress tensor
 Ω magnitude of vorticity tensor, Eq. (25)
 Ω_{ij} vorticity tensor, Eq. (26)

REFERENCES

- [1] Youngren, H., and Drela, M., 1991, "Viscous/Inviscid Method for Preliminary Design of Transonic Cascade," AIAA-91-2364, pp.1-11.
 [2] Chima, R. V., 1985, "Inviscid and Viscous Flows in Cascades with an Explicit Multiple-Grid Algorithm," AIAA Journal, **23**(10), pp. 1556-1563.

- [3] Giles, M. B., 1990, "Nonreflecting Boundary Conditions for Euler Equation Calculations," *AIAA Journal*, **28**(12), pp. 2050-2058.
- [4] Shimada, M., and Nagano, Y., 1996, "Advanced two-equation turbulence model for complex flows in engineering," *Engineering Turbulence Modeling and Measurements* **3**, Elsevier, pp.111-120.
- [5] Senoo, S., Shikano, Y., Ikeguchi, T., and Segawa, K., 1998, "Three-dimensional Turbulent Flow Analysis through Turbine Blades," *Proc. 4th KSME-JSME Fluid Engineering Conference*, pp. 197-200.
- [6] Chakravarthy, S.R. and Osher, S., 1985, "A New Class of High Accuracy TVD Schemes for Hyperbolic Conservation Laws," *AIAA Paper* 85-0363.
- [7] Pulliam, T. H. and Chaussee, D. S., 1981, "A Diagonal Form of an Implicit Approximate-Factorization Algorithm," *J. Comp. Phys.*, **39**, p. 347.
- [8] Steger, J.L., and Sorenson, R.L., 1979, "Automatic Mesh-Point Clustering near a Boundary in Grid Generation with Elliptic Partial Differential Equations," *Journal of Computational Physics*, **33**, pp.405-410.
- [9] Giles, M. B., 1988, "UNSFLO: A Numerical Method for Unsteady Inviscid Flow in Turbomachinery," *Gas Turbine Lab., Massachusetts Institute of Technology, Cambridge, MA*, TR 195, pp.1-92.
- [10] Schreiber, H.A., and Starke, H., 1984, "Experimental Cascade Analysis of a Transonic Compressor Rotor Blade Section," *ASME Journal of Engineering for Gas Turbines and Power*, **106**, pp.288-294.
- [11] Tweedt, D.L., Schreiber, H.A., and Starke, H., 1988, "Experimental Investigation of the Performance of a Supersonic Compressor Cascade," *ASME Journal of Turbomachinery*, **110**, pp.456-466.